optica

Controlled switching of orbital angular momentum in an optical parametric oscillator

A. Aadhi,[1,*] G. K. Samanta,[1] S. Chaitanya Kumar,[2] and M. Ebrahim-Zadeh[2,3]

[1]Photonic Sciences Lab., Physical Research Laboratory, Navarangpura, Ahmedabad 380009, Gujarat, India
[2]ICFO-Institut de Ciencies Fotoniques, The Barcelona Institute of Science and Technology, 08860 Castelldefels (Barcelona), Spain
[3]ICREA, Passeig Lluis Companys 23, Barcelona 08010, Spain
*Corresponding author: aadhi@prl.res.in

Received 6 December 2016; revised 6 February 2017; accepted 9 February 2017 (Doc. ID 282327); published 7 March 2017

Controlled switching of orbital angular momentum (OAM) of light at practical powers over arbitrary wavelength regions can have important implications for future quantum and classical systems. Here we report on a single source of OAM beams based on an optical parametric oscillator (OPO) that can provide all such capabilities. We demonstrate active transfer of OAM modes of any order, $|l_p|$, of *pump* to the *signal* and *idler* in an OPO, to produce $|l_p|+1$ different OAM states by controlling the relative cavity losses of the resonated beams. As a proof-of-principle, we show that when pumping with the OAM states $|l_p| = 1$ and $|l_p| = 2$ for different relative losses of signal and idler, the OPO has two ($|1,0\rangle$ and $|0,1\rangle$) and three ($|2,0\rangle$, $|1,1\rangle$, and $|0,2\rangle$) output states, respectively. Our findings show that using a suitable loss modulator, one can achieve rapid switching of the OAM mode in OPO output beams in time.

OCIS codes: (190.4970) Parametric oscillators and amplifiers; (190.4223) Nonlinear wave mixing; (190.4410) Nonlinear optics, parametric processes; (260.6042) Singular optics; (050.4865) Optical vortices; (190.4360) Nonlinear optics, devices.

https://doi.org/10.1364/OPTICA.4.000349

1. INTRODUCTION

Like polarization and wavelength, orbital angular momentum (OAM) of light provides an additional degree of freedom, which could be of great benefit for many applications from quantum mechanics to optical communication. Optical vortex beams with a doughnut intensity distribution, due to phase singularities (dislocations) in the wavefront, carry OAM. The characteristic phase distribution of optical vortices is given by $\exp(\pm il\theta)$, where θ is the azimuthal angle and the integer, l, known as topological charge or vortex order, indicates the OAM carried by each photon in the beam. The sign ($\pm$) of l is the direction of rotation of the helical wavefront along the propagation direction. Since the discovery of OAM in optical vortices [1], such beams have found applications in micro-manipulation [2,3], high-resolution lithography [4,5], microscopy [6,7], interferometry [8,9], and classical and quantum communications [10,11]. However, to exploit the extra degree of freedom provided by OAM for new intriguing applications in classical and quantum communications, it is essential to further develop novel systems that can rapidly control and switch the OAM modes of light at arbitrary wavelengths. We show that such a unique capability can be provided by an optical parametric oscillator (OPO).

Typically, OAM beams are generated through spatial phase modulation of Gaussian beams using spiral phase plates (SPPs) [12,13], spatial light modulators (SLM) [14], Q-plates [15], or cylindrical lens mode convertors [16]. However, due to intrinsic limitations, none of the existing techniques can provide high power in higher-order vortex beams or at arbitrary wavelengths. For example, SPPs can be used for high-power operation, but material dispersion and limitations in fabrication technology limit their utility to discrete wavelengths and lower vortex orders. Similarly, SLMs and Q-plates produce vortices over wider wavelength regions, but a low damage threshold restricts their use to low powers. Cylindrical mode converters can provide high power and wide spectral coverage, but the generation of higher-order vortices is limited by the difficult requirement of higher-order Hermite–Gaussian modes as inputs [16]. Based on OAM conservation in nonlinear interactions, frequency conversion experiments have recently generated high-power and higher-order optical vortices at new but discrete wavelengths [13,17,18].

OPOs are recognized as versatile sources of coherent radiation providing high power and broad wavelength coverage from a single device, in all time-scales from continuous-wave (cw) to the femtosecond domain [19–21]. Therefore, direct generation and control of OAM modes in an OPO can offer an intriguing route to provide high-power OAM beams at arbitrary wavelengths. Previous efforts [22–25] have confirmed the possibility of generating OAM beams from OPOs, where it was shown that the transfer of OAM from the pump to the output beams was dictated by cavity detuning and anisotropic cavity mode propagation due to crystal birefringence [25]. Therefore, without active control, the transfer of OAM from the pump is constrained to only

one of the output beams. To realize active control and transfer of the OAM in an OPO, it is thus essential to understand the mechanism of OAM exchange among the interacting beams in such a system.

Here we report the first demonstration of an OPO with active control of OAM, producing cw radiation with OAM modes across 949.5–1209.7 nm. Unlike pulsed OPOs, the generation of OAM beams using cw OPOs is challenging due to low parametric gain and high threshold sensitivity to cavity losses. Hence, to induce coherent amplification of oscillating OAM modes, it is imperative to maintain high gain and low cavity losses in the OPO. To this end, we deploy a doubly-resonant oscillator (DRO) and a quasi-phase-matched (QPM) nonlinear crystal to achieve high gain and avoid anisotropy effects due to birefringence [25]. We theoretically predict and experimentally verify that the relative cavity losses for the resonated signal and idler determine the transfer of pump OAM to one or the other beam. Therefore, by controlling cavity losses, one can selectively switch the OAM state of the pump to either signal or idler. As such, owing to the parity of the resonator in presence of isotropic propagation in the QPM crystal, one can generate $|l_p|+1$ OAM state combinations in the OPO output using a single pump OAM state, $|l_p\rangle$. As a proof-of-principle, pumping the OPO with OAM states $|l_p| = 1$ and $|l_p| = 2$ and controlling the relative signal and idler cavity losses, we generate the output states ($|1, 0\rangle$ and $|0, 1\rangle$) and ($|2, 0\rangle$ and $|1, 1\rangle$), respectively. For 3.2 W of green pump power with $l_p = 1$, the output in one of the OAM states varies from 77 to 125 mW for signal (idler) from 1060.37 nm (1067.7 nm) to 949.62 nm (1209.7 nm), with total power of 240 mW at 965.3 nm (1185 nm).

2. THEORETICAL BACKGROUND

To understand the OAM transfer mechanism, we evaluate the spatial overlap integral of the pump, signal, and idler in a nonlinear medium, given by

$$\Lambda_{l_p,l_s,l_i} \propto \left| \int E_p E_s^* E_i^* \mathrm{d}s \right| \propto \left| \int_0^{2\pi} \exp(i(l_p - l_s - l_i)\varphi)\mathrm{d}\varphi \right|, \quad (1)$$

where E_p, E_s, and E_i are electric fields and l_p, l_s, and l_i are OAM modes of the interacting beams. The subscripts p, s, and i refer to pump, signal, and idler, respectively. From Eq. (1), it is evident that the overlap integral, Λ_{l_p,l_s,l_i}, has maximum value for $l_p = l_s + l_i$. Hence, for a fixed pump mode, the signal and idler can have all possible combinations of transverse modes, but cavity parity restricts the number of oscillating transverse modes for a given longitudinal mode [25]. In our experiment, the QPM crystal enables isotropic propagation of cavity modes in the gain medium. Thus, for the pump modes $l_p = 1$ and $l_p = 2$, having odd and even parity, respectively, the oscillating signal and idler modes should have opposite and the same parity, respectively, to have a non-zero overlap integral. Hence, for $l_p = 1$, if the signal carries the OAM mode $l_s = 1$, then the idler will have $l_i = 0$ (Gaussian mode), and vice versa, resulting in two equally probable output OAM states, $|l_s, l_i\rangle = |1, 0\rangle$ and $|0, 1\rangle$, with an estimated normalized overlap integral $\eta_{l_p,l_s,l_i} = \eta_{1,1,0} = \eta_{1,0,1} \sim 0.7$. Similarly, for $l_p = 2$, there are three equally probable output OAM states given by $|l_s, l_i\rangle = |1, 1\rangle$, $|2, 0\rangle$, and $|0, 2\rangle$, with estimated normalized overlap integral $\eta_{l_p,l_s,l_i} = \eta_{2,1,1} \sim 0.7$ and $\eta_{l_p,l_s,l_i} = \eta_{2,2,0} = \eta_{2,0,2} \sim 0.5$, respectively. However, for selective excitation of a specific pair of signal and idler OAM modes, one needs to solve dynamic equations [25,26] of the OPO under different experimental conditions. For simplicity, we consider the DRO pumped with OAM mode, $l_p = 1$, resulting in two operating conditions. In Case-I, pump OAM is transferred to signal, and the idler oscillates in fundamental transverse mode, resulting in the output OAM state, $|1, 0\rangle$. In Case-II, the signal oscillates in fundamental transverse mode, and the pump OAM is transferred to the idler, resulting in the output OAM state $|0, 1\rangle$. Using similar mathematical treatment as in Refs. [25,26], we find that in the steady state, the parametric oscillation thresholds for the DRO in Case-I and Case-II are, respectively, given by

$$x_{\mathrm{in}}^2 = \frac{\tilde{\gamma}_s}{\eta}, \quad (2)$$

and

$$x_{\mathrm{in}}^2 = \frac{\tilde{\gamma}_i}{\eta}. \quad (3)$$

All variables in Eqs. (2) and (3) are defined as follows [26], after normalization with respect to cavity round trip time, τ:

$$x_{\mathrm{in}} = \chi \Lambda_{l_p,l_s,l_i} \tau^2 E_{\mathrm{in}},$$
$$\tilde{\gamma}_s = \gamma_s \tau, \tilde{\gamma}_i = \gamma_i \tau,$$
$$\eta = \eta_{l_p,l_s,l_i} = \frac{\Lambda_{l_p,l_s,l_i}}{\Lambda_{0,0,0}}. \quad (4)$$

Here, E_{in} is the input electric field, χ is the nonlinear coupling constant, γ_s and γ_i are cavity losses for the signal and idler, respectively, and $\Lambda_{0,0,0}$ is the spatial overlap integral for the pump, signal, and idler in the Gaussian profile. From Eqs. (2) and (3), it is evident that in isotropic propagation (QPM crystal), excitation of the cavity modes for the oscillating signal and idler beams in the DRO are governed by the losses. If the signal loss, γ_s, is lower (higher) than the idler loss, γ_i, the DRO cavity will support oscillation of the signal (idler) in the vortex (Gaussian) mode, carrying the OAM. Therefore, by switching the cavity losses for signal and idler, one can selectively transfer the OAM mode of the pump to signal or idler.

3. EXPERIMENT

The schematic of the experimental setup for vortex-pumped OPO is shown in Fig. 1(a). A 50 W, cw Yb-fiber laser [27] (IPG Photonics, YLR-50-1064) delivering single-frequency radiation at 1064 nm in a linearly polarized beam with a Gaussian spatial profile ($M^2 < 1.07$) is used as the fundamental pump source. The laser is frequency-doubled to 532 nm in the green using a 30-mm-long MgO-doped stoichiometric $LiTaO_3$ (MgO:sPPLT) crystal (C1) with a 1 mm × 1 mm aperture that contains a single grating period ($\Lambda = 7.97$ μm) [28] to provide the pump radiation for the OPO. A lens, L1, of focal length, $f = 100$ mm, is used to focus the fundamental at the center of the MgO:sPPLT crystal (C1) to a beam waist radius of ~42 μm, corresponding to the focusing parameter, $\xi \sim 2.88$, for optimum SHG efficiency. The green source has similar performance in terms of output power, beam profile, and power stability to our previous report [29]. A wavelength separator, S1, extracts the green radiation from the fundamental. Because doubly-resonant OPOs have low thresholds, we limited the fundamental power to 25 W, generating 5.6 W of green radiation at 532 nm in a Gaussian beam profile ($M^2 < 1.02$) with power stability of 2.2% rms over 4 h. The green beam in Gaussian

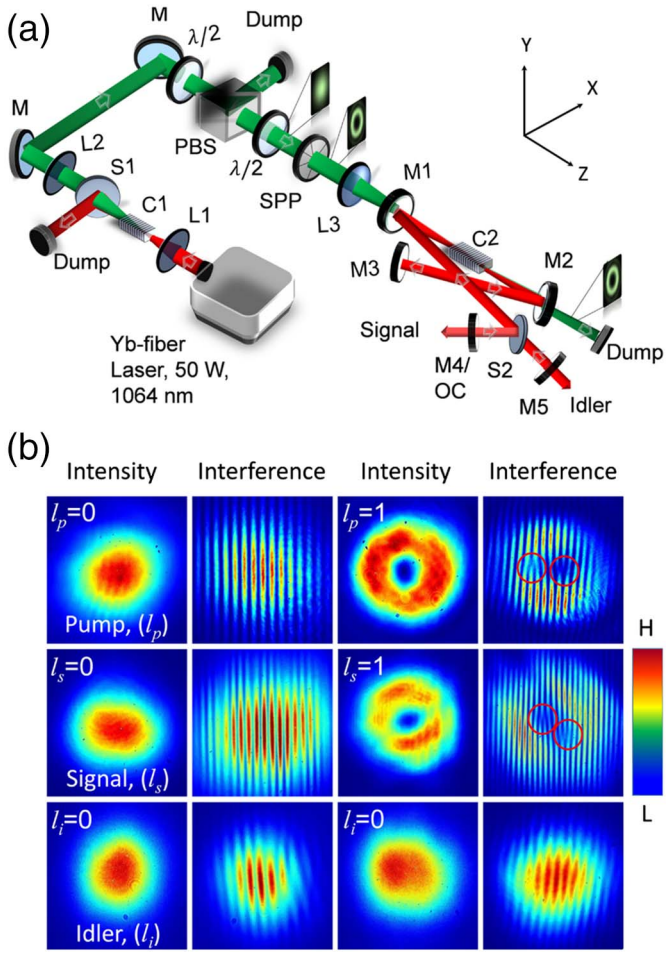

Fig. 1. OAM-mode-pumped doubly-resonant OPO. (a) Schematic of the experimental setup. The 50 W cw Yb-fiber laser. $\lambda/2$, half-wave plates; PBS, polarizing beam splitter cube; L1–L3, lenses; SPP, spiral phase plate; C1–C2, nonlinear crystals for frequency doubling and DRO operation, respectively. S1–S2, wavelength separators; M, folding mirrors at green wavelength; M1–M5, DRO mirrors; and OC, output coupler. (b) Intensity profile of pump, signal, and idler beams for pump OAM mode $l_p = 0$ (first column) and $l_p = 1$ (third column). Corresponding interference patterns in second and third columns.

spatial profile is collimated using a lens, L2, of focal length, $f = 200$ mm. The conventional power attenuator [27], comprised of a polarizing beam splitter (PBS) and a half-wave plate ($\lambda/2$), controls the green power to the OPO. However, for perfect phase-matching, the polarization of the input beam is further adjusted using a second $\lambda/2$ plate depending upon the orientation of the nonlinear crystal. A SPP is an optical element with a helically varying optical path length, which is used to convert the Gaussian pump beam into an optical vortex. The thickness of the element is engineered to have an azimuthal phase distribution from 0 to $2\pi l$. Using the SPP [30] of phase winding number $l = 1$ and 2, the Gaussian green pump beam is converted into an optical vortex beam of orders $l_p = 1$ and 2, respectively, at >95% efficiency. A lens, L3, of focal length, $f = 150$ mm, is used to focus green beam of orders $l_p = 0$, 1, and 2, at the center of the nonlinear crystal. Here, $l_p = 0$ signifies the Gaussian beam. A 30-mm-long MgO:sPPLT [28] crystal (C2) with a 2 mm × 1 mm aperture containing a single grating period ($\Lambda = 7.97$ μm) is used for OPO operation. In the present study, we used two different DRO configurations. First, a four-mirror ring cavity (not shown in the current paper) was used, where both signal and idler oscillate along the same path in the cavity. Such a configuration was used to achieve low cavity losses and the lowest DRO threshold. However, to control feedback losses at the signal and idler separately, for selective transfer of pump OAM to either beam, we later configured a five-mirror standing-wave cavity [see Fig. 1(a)] with a wavelength separator, S2, (high reflectivity at signal; high transmission at idler) to resonate the signal and idler along two different paths. In both configurations, we used two plano-concave mirrors (M1–M2) with a radius of curvature $r = 150$ mm, and two (M3–M4) and three (M3–M5) plane mirrors in ring and standing-wave cavities, respectively. All mirrors have high transmission ($T > 90\%$) at the pump wavelength (532 nm) and high reflectivity ($R > 95\%$) across the signal and idler wavelength range (950–1200 nm), ensuring DRO operation. Both nonlinear crystals, C1 and C2, are housed in an oven, which can be adjusted up to 200°C with a temperature stability of ±0.1°C. The total optical length of the ring and standing-wave cavity are 592 and 952 mm, respectively.

4. RESULTS AND DISCUSSION

To study exchange of OAM among interacting photons, we operated the DRO in a ring cavity at a signal (idler) wavelength of 1000 nm (1137 nm), away from degeneracy. Pumping the OPO with ~3.2 W of the green beam with two different vortex orders $l_p = 0$ and $l_p = 1$ separately, we recorded the intensity profiles of pump, signal, and idler, with the results shown in Fig. 1(b). As evident from first column of Fig. 1(b), for the pump beam of vortex order $l_p = 0$ both signal and idler beams have similar intensity profiles to pump. For further confirmation, we performed interference experiments by self-interfering the pump, signal, and idler in a Mach–Zehnder interferometer and recorded the respective interference patterns, with the results shown in second column of Fig. 1(b). From the straight-line interference fringes, it is evident that none of the beams carry any phase singularity. As expected, for pump beam of vortex order, $l_p = 0$ (Gaussian), both signal and idler also have Gaussian intensity distribution ($l_p = 0$). However, for pump beam of vortex order, $l_p = 1$, the signal and idler beams have doughnut and Gaussian intensity profiles, respectively [see third column of Fig. 1(b)]. To confirm the vortex order (OAM mode) of the beams, we once again performed self-inference experiments in a Mach–Zehnder interferometer and obtained the patterns shown in fourth column of Fig. 1(b). The fork pattern, as marked with red circles in the interferogram of pump and signal, confirms that both beams carry OAM, characteristic of optical vortex. The order of the pump and signal vortices are $l_p = 1$ and $l_s = 1$, respectively. Alternatively, the straight-line interference pattern for the idler confirms no phase singularity or OAM mode, with $l_i = 0$. From this study, it is evident that the vortex order of the pump (l_p) is equal to the sum of the vortex orders of the generated signal (l_s) and idler (l_i) beams, confirming the conservation of OAM in an OPO. However, it is interesting to note that the OAM of the pump is only transferred to the signal and not to the idler radiation, resulting in an output OAM state, $|l_s, l_i\rangle = |1, 0\rangle$, although both $|1, 0\rangle$ and $|0, 1\rangle$ are equally probable output states of the OPO. Unlike previous reports [23–25], the use of QPM

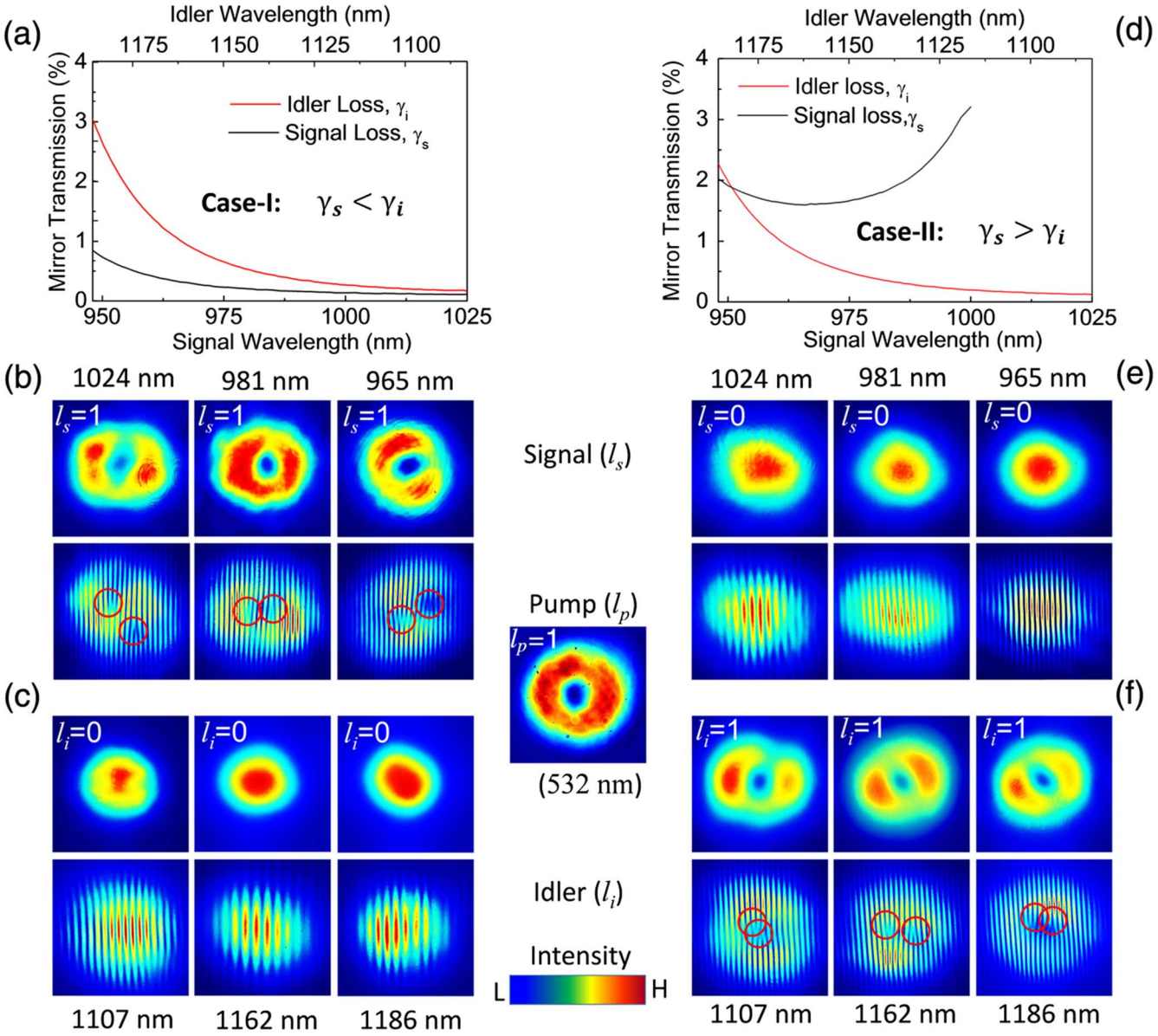

Fig. 2. Controlled switching of OAM mode of pump to the generated beams in an OPO. Variation of feedback losses for signal and idler across the tuning range of the OPO. (a) Signal loss lower than idler loss (Case-I). (d) Signal loss higher than idler loss (Case-II). Intensity distribution (first row) and self-interference pattern (second row) of (b) the signal beam, and (c) corresponding idler beam across the tuning range of the DRO for Case-I. Similarly, the intensity distribution (first row) and self-interference pattern (second row) of (e) the signal beam, and (f) corresponding idler beam across the tuning range of the DRO for Case-II.

crystal here eliminates the role of anisotropy due to birefringence in transferring OAM to the signal radiation.

According to Eqs. (2) and (3), the OAM transfer mechanism in a DRO with a QPM crystal (isotropic mode propagation) is determined by the losses of the resonated beams. To control the respective losses, we operated the DRO in a standing-wave cavity [see Fig. 1(a)] with the signal and idler oscillating along two different paths formed by the separator, S2. The resonating signal and idler share the same cavity, except mirrors, M4 and M5, enabling independent control of signal and idler feedback, respectively. With all cavity mirrors, including M4 and M5, highly reflecting, the signal loss was lower than idler loss ($\gamma_s < \gamma_i$) across the full DRO tuning range [see Fig. 2(a)], corresponding to Case-I. However, by controlling the signal output coupling through M4, we could achieve a lower loss at the idler than signal ($\gamma_i < \gamma_s$) across nearly the full DRO tuning range [see Fig. 2(d)], corresponding to Case-II. When pumping the DRO with vortex beam of order $l_p = 1$ in Case-I, the signal beam, tunable across 965–1024 nm, has a doughnut-shaped intensity distribution [see first row of Fig. 2(b)], carrying the OAM mode of order $l_s = 1$. This is further confirmed by the characteristic fork interference pattern (see red circles), as shown in second row of Fig. 2(b), obtained by self-interference of the beam in a Mach–Zehnder interferometer. The corresponding idler beam, tunable across 1185–1107 nm, has Gaussian intensity distribution, $l_i = 0$ [see first row of Fig. 2(c)], also confirmed by the straight-line interference patterns, as shown in second row of Fig. 2(c). The resultant output state of the DRO is thus $|l_s, l_i\rangle = |1, 0\rangle$.

However, when we replace M4 with an output coupler [31], which, together with the transmission of S2 at <20° angle of incidence, results in a signal transmission profile as shown in Fig. 2(d), the signal experiences a higher loss than idler ($\gamma_s > \gamma_i$) across nearly the entire DRO tuning range, corresponding to Case-II. Under this condition, the signal beam adopts a Gaussian intensity distribution, $l_s = 0$ [see first row of Fig. 2(e)], which is further confirmed by the straight-line interference pattern shown in second row of Fig. 2(e). Alternatively, the corresponding idler beam across the tuning range now has a doughnut-shaped intensity profile [see first row of Fig. 2(f)], carrying OAM mode, $l_i = 1$, further confirmed by the characteristic fork interference pattern (see red circles) shown in second row of Fig. 2(f). The resultant output state of the DRO is now $|l_s, l_i\rangle = |0, 1\rangle$. In addition to mirror transmission losses, the overall loss can also be modulated by reduced amplification using cavity misalignment. Since the beams with non-integer multiples of OAM per photon have neither circular symmetry nor propagate in a structurally stable fashion [32], unlike Ref. [24], we do not observe any fractional vortex beam from the DRO. However, when the DRO is operated near degeneracy, with identical signal and idler losses [see mirror transmission in Fig. 2(a)], both beams can, in principle, carry the OAM mode of the pump with equal probability. In addition, due to the relatively high gain at degeneracy and identical operation threshold for both signal and idler, the OPO is expected to oscillate in multimode or mixed spatial modes. As a result, neither beam has a stable OAM mode structure. The DRO oscillation threshold for the output OAM states, $|1, 0\rangle$ and $|0, 1\rangle$, is measured to be 0.77 and 1.56 W, respectively. The higher threshold for state $|0, 1\rangle$ is attributed to the higher total cavity loss due to the output coupler. While studying the stability of the output beams, we observed fluctuation in the intensity profile of the beams over time. Such intensity fluctuations are attributed to thermal effects, mechanical vibrations, and the air currents in our laboratory. However, it is interesting to note that the interference pattern of both the signal and idler vortex beams show a stable pattern over time, confirming the stable phase structure of the output beams.

To further understand the transfer of pump OAM mode to signal and idler, we operated the DRO in a standing-wave cavity including mirrors, M4 and M5, at a signal (idler) wavelength of 981 nm (1162 nm). We then pumped the DRO by a vortex beam of order $l_p = 2$ and recorded the intensity profile of signal and idler, as shown in Fig. 3. Figure 3(a) demonstrates the intensity profile of the pump beam of order $l_p = 2$, as confirmed by the fork (see red circles) interference pattern. In general, both signal and idler have doughnut intensity distributions [see first row of Fig. 3(b)], with OAM modes of $l_s = 1$ and $l_i = 1$, respectively. This is also confirmed by the fork (see red circle) interference pattern [see second row of Fig. 3(b)], resulting in the output OAM state, $|l_s, l_i\rangle = |1, 1\rangle$. Even with lower cavity loss for signal than idler [see the mirror transmission in Fig. 2(a)], both beams oscillate in vortex modes due to higher nonlinear gain arising from stronger mode coupling, η_{l_p,l_s,l_i}, among the interacting beams for identical modes [26]. The DRO threshold for the output state, $|1, 1\rangle$, is measured to be 1.56 W, even with highly reflecting cavity mirrors. The higher threshold is attributed to the reduction in parametric gain with the order of pump vortex [17]. Therefore, to transfer the pump OAM mode to either the signal or idler, the cavity losses for idler or signal must be increased, respectively.

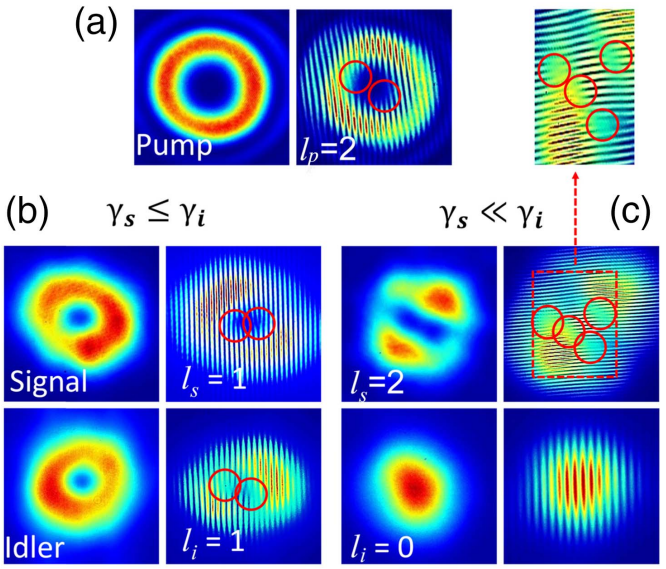

Fig. 3. OAM mode sharing among signal and idler beams for pump OAM mode $l_p = 2$. (a) Intensity distribution and interference pattern of the pump beam with OAM mode $l_p = 2$. Intensity distribution and interference pattern of the signal (first row) and corresponding idler (second row) for signal and idler feedback losses satisfying (b) $\gamma_s \leq \gamma_i$ and (c) $\gamma_s \ll \gamma_i$.

However, with vortex pump beam of order $l_p = 2$ operation of the DRO could not be achieved due to the unavailability of appropriate output coupler with the signal transmission in place of M4. Since the operation of OPO is highly influenced by nonlinear gain and cavity losses, change in any of these two parameters can change the OAM transfer mechanism in the OPO. For fixed laser power and crystal parameters, the nonlinear gain and the cavity loss can be varied through the spatial overlapping of the interacting beams through cavity misalignment and the transmission of the cavity mirrors, respectively. Therefore, we used the same cavity configuration, but slightly offset the alignment of mirror, M5 [see Fig. 1(a)], to transfer the OAM mode of the pump to the signal, and then recorded the intensity profile of signal and idler. The results are shown in first column of Fig. 3(c), where the signal (idler) beam has a doughnut (Gaussian) intensity distribution, carrying OAM mode of $l_s = 2(l_i = 0)$, as was also confirmed by the characteristic fork (straight-line) interference pattern shown in the second column of Fig. 3(c), resulting in the output OAM state $|2, 0\rangle$. However, we note that due to the asymmetry caused by the cavity misalignment and instability of higher-order vortices [17], the signal beam

Table 1. Controlled OAM Mode Switching in a Doubly-Resonant OPO

	OAM			Output OAM State
Control Relative Loss[a]	Pump $\|l_p\rangle$	$\|l_s\rangle$	$\|l_i\rangle$	$\|l_s,l_i\rangle$
$\gamma_s < \gamma_i$	1	1	0	$\|1, 0\rangle$
$\gamma_s > \gamma_i$	1	0	1	$\|0, 1\rangle$
$\gamma_s \leq \gamma_i$	2	1	1	$\|1, 1\rangle$
$\gamma_s \ll \gamma_i$	2	2	0	$\|2, 0\rangle$
$\gamma_s \gg \gamma_i$	2	0	2	$\|0, 2\rangle$

[a]Loss of signal ($\tilde{\gamma}_s$) and idler ($\tilde{\gamma}_i$) are controlled by changing the cavity mirrors with different transmission and also by cavity misalignment.

OAM mode disintegrated into two unit charged OAM modes. The DRO threshold for such an output OAM state of $|2, 0\rangle$ is 2.1 W, significantly higher than the output states. Similarly, one can expect the transfer of pump order $l_p = 2$ to the idler radiation to produce the output OAM state $|0, 2\rangle$ through proper selection of cavity losses. However, due to the unavailability of suitable mirrors for the idler in our laboratory, we could not access this output state. To better understand how DRO operation generates different output OAM states, we have tabulated all the experimental parameters in Table 1. From the table, it is evident that the selective transfer of the pump OAM mode to the output beams of an OPO can be realized by controlling relative cavity losses, in agreement with our theoretical predictions.

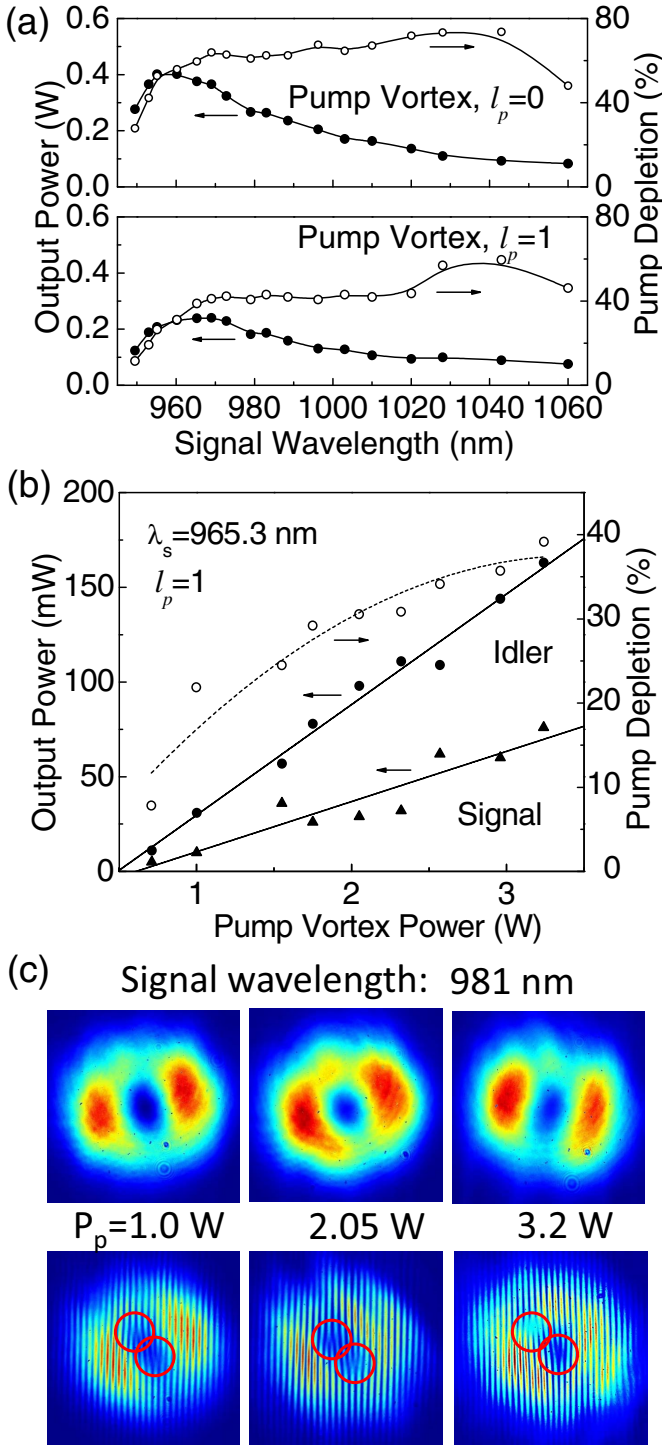

Fig. 4. Performance characterization of the vortex-pumped cw DRO source. (a) Variation of output power of the DRO for pump OAM modes $l_p = 0$ (Gaussian) and $l_p = 1$ across the tuning range. (b) Power-scaling characteristics of the DRO source with pump vortex $l_p = 1$. (c) Intensity (first row) pattern of the signal OAM mode and corresponding fork (see red circles) interference pattern (second row) for different pump powers.

To evaluate the practical utility of the new vortex source for potential applications, we further characterized the performance of the DRO with regard to output power and efficiency across the tuning range. We pumped the DRO in the ring cavity configuration with green power of 3.2 W and measured the total output power (signal plus idler) across the tuning range for a pump beam with a Gaussian spatial profile, $l_p = 0$, and a vortex profile, $l_p = 1$. The results are shown in Fig. 4(a). For the Gaussian pump beam, the DRO produces a maximum output power of 400 mW at a signal (idler) wavelength of 960.2 nm (1192.9 nm) with a pump depletion of up to 73% at a signal (idler) wavelength of 1043 nm (1085.8 nm). The variation in the output power is attributed to the varying transmission of the cavity mirrors. When pumping with the optical vortex beam, the DRO generates a lower output power of 240 mW with a reduced pump depletion of 60%, due to the lower parametric gain with an optical vortex than a Gaussian pump beam. We also studied power scaling of the vortex-pumped DRO at a signal wavelength of 965.3 nm (crystal temperature of $T = 90°C$). Varying the vortex pump power, we recorded the total output power and pump depletion, showing the results in Fig. 4(b). At 3.2 W of pump power, the DRO generates a maximum total power of 240 mW, with 75 mW of signal power in the vortex beam profile at a slope efficiency of 2.6%, and 165 mW of idler in Gaussian beam profile at a slope efficiency of 5.8%. We further recorded the intensity profile of the signal beam for three different pump powers, $P_p = 1$, 2.05, and 3.2 W, with the results shown in Fig. 4(c). As evident from the first row of Fig. 4(c), the signal beam has a doughnut-shaped intensity profile carrying the OAM mode $l_s = 1$, which is further confirmed from the characteristic fork (see red circles) interference pattern shown in second row of Fig. 4(c). The deterioration of signal beam intensity pattern from the doughnut shape with the increase in pump power from 1 to 3.2 W, evident in first row of Fig. 4(c), can be attributed to the excitation of higher-order cavity modes due to enhancement of nonlinear gain at higher pump powers.

5. CONCLUSIONS

In conclusion, we have reported the first demonstration of controlled switching of an OAM mode of light using an OPO. This is also the first report of a vortex-pumped cw OPO. Using a DRO, we have shown that by controlling relative losses of the resonant beams, the OAM mode of pump can be selectively transferred to either of the generated beams or shared between them. Hence, for an OAM of l, we can produce $l + 1$ signal and idler output OAM states, $|l_s, l_i\rangle$. Pumping the DRO with OAM modes, $l_p = 1$ and $l_p = 2$, we generated output states of $|1, 0\rangle$ and $|0, 1\rangle$ and $|1, 1\rangle$, $|2, 0\rangle$, and $|0, 2\rangle$, respectively, with up to 240 mW across 946–1200 nm. This generic technique thus enables controlled transfer and switching of OAM at practical powers, in all timescales, and at arbitrary wavelengths from visible to mid-infrared,

and it can also produce higher-order vortices using a higher-order vortex pump beam.

Funding. Ministerio de Economía y Competitividad (MINECO) (TEC2015-68234-R); European Commission (EC) (H2020- MSCA-ITN-2014); Severo Ochoa Excellence Grant (SEV-2015-0522); Fundacio Privada Cellex.

REFERENCES

1. L. Allen, M. W. Beijersbergen, R. J. Spreeuw, and J. P. Woerdman, "Orbital angular momentum of light and the transformation of Laguerre–Gaussian laser modes," Phys. Rev. A **45**, 8185–8189 (1992).
2. D. G. Grier, "A revolution in optical manipulation," Nature **424**, 810–816 (2003).
3. M. Padgett and R. Bowman, "Tweezers with a twist," Nat. Photonics **5**, 343–348 (2011).
4. T. F. Scott, B. A. Kowalski, A. C. Sullivan, C. N. Bowman, and R. R. McLeod, "Two-color single-photon photo-initiation and photo-inhibition for sub-diffraction photolithography," Science **324**, 913–917 (2009).
5. Z. Gan, Y. Cao, R. A. Evans, and M. Gu, "Three-dimensional deep sub-diffraction optical beam lithography with 9 nm feature size," Nat. Commun. **4**, 2061 (2013).
6. S. Bernet, A. Jesacher, S. FŘrhapter, C. Maurer, and M. Ritsch-Marte, "Quantitative imaging of complex samples by spiral phase contrast microscopy," Opt. Express **14**, 3792–3805 (2006).
7. S. Fürhapter, A. Jesacher, S. Bernt, and M. Ritsch-Marte, "Spiral phase contrast imaging in microscopy," Opt. Express **13**, 689–694 (2005).
8. S. Furhapter, A. Jesacher, S. Bernet, and M. Ritsch, "Spiral interferometry," Opt. Lett. **30**, 1953–1955 (2005).
9. G. Foo, D. M. Palacios, and G. A. Swartzlander, "Optical vortex coronagraph," Opt. Lett. **30**, 3308–3310 (2005).
10. Y. Yan, G. Xie, M. P. Lavery, H. Huang, N. Ahmed, C. Bao, L. Li, Z. Zhao, A. F. Molisch, M. Tur, M. J. Padgett, and A. E. Willner, "High-capacity millimetre-wave communications with orbital angular momentum multiplexing," Nat. Commun. **5**, 4876 (2014).
11. A. Mair, A. Vaziri, G. Weihs, and A. Zeilinger, "Entanglement of the orbital angular momentum states of photons," Nature **412**, 313–316 (2001).
12. S. S. R. Oemrawsingh, J. A. W. van Houwelingen, E. R. Eliel, J. P. Woerdman, E. J. K. Verstegen, J. G. Kloosterboer, and G. W. t'Hooft, "Production and characterization of spiral phase plates for optical wavelengths," Appl. Opt. **43**, 688–694 (2004).
13. N. Apurv-Chaitanya, S. Chaitanya Kumar, K. Devi, G. K. Samanta, and M. Ebrahim-Zadeh, "Ultrafast optical vortex beam generation in the ultraviolet," Opt. Lett. **41**, 2715–2718 (2016).
14. M. Zürch, C. Kern, P. Hansinger, A. Dreischuh, and C. Spielmann, "Strong-field physics with singular light beams," Nat. Phys. **8**, 743–746 (2012).
15. L. Marrucci, C. Manzo, and D. Paparo, "Optical spin-to-orbital angular momentum conversion in inhomogeneous anisotropic media," Phys. Rev. Lett. **96**, 163905 (2006).
16. M. W. Beijersbergen, L. Allen, H. Van der Veen, and J. P. Woerdman, "Astigmatic laser mode converters and transfer of orbital angular momentum," Opt. Commun. **96**, 123–132 (1993).
17. N. Apurv-Chaitanya, A. Aadhi, M. V. Jabir, and G. K. Samanta, "Frequency-doubling characteristics of high-power, ultrafast vortex beams," Opt. Lett. **40**, 2614–2617 (2015).
18. N. V. Bloch, K. Shemer, A. Shapira, R. Shiloh, I. Juwiler, and A. Arie, "Twisting light by nonlinear photonic crystals," Phys. Rev. Lett. **108**, 233902 (2012).
19. M. Ebrahim-Zadeh, S. Chaitanya Kumar, A. Esteban-Martin, and G. K. Samanta, "Breakthroughs in photonics 2012: breakthroughs in optical parametric oscillators," IEEE Photon. J. **5**, 0700105 (2013).
20. G. K. Samanta, A. Aadhi, and M. Ebrahim-Zadeh, "Continuous-wave, two-crystal, singly-resonant optical parametric oscillator: theory and experiment," Opt. Express **21**, 9520–9540 (2013).
21. A. Aadhi, N. Apurv Chaitanay, M. V. Jabir, R. P. Singh, and G. K. Samanta, "All-periodically poled, high-power, continuous-wave, single-frequency tunable UV source," Opt. Lett. **40**, 33–36 (2015).
22. A. Smith and D. Armstrong, "Generation of vortex beams by an image-rotating optical parametric oscillator," Opt. Express **11**, 868–873 (2003).
23. A. Abulikemu, T. Yusufu, R. Mamuti, K. Miyamoto, and T. Omatsu, "Widely-tunable vortex output from a singly resonant optical parametric oscillator," Opt. Express **23**, 18338–18344 (2015).
24. K. Miyamoto, S. Miyagi, M. Yamada, K. Furuki, N. Aoki, M. Okida, and T. Omatsu, "Optical vortex pumped mid-infrared optical parametric oscillator," Opt. Express **19**, 12220–12226 (2011).
25. M. Martinelli, J. A. Huguenin, P. Nussenzveig, and A. Z. Khoury, "Orbital angular momentum exchange in an optical parametric oscillator," Phys. Rev. A **70**, 013812 (2004).
26. C. Schwob, P. F. Cohadon, C. Fabre, M. A. Marte, H. Ritsch, A. Gatti, and L. Lugiato, "Transverse effects and mode couplings in OPOs," Appl. Phys. B **66**, 685–699 (1998).
27. A. Aadhi, N. Apurv Chaitanya, M. V. Jabir, P. Vaity, R. P. Singh, and G. K. Samanta, "Airy beam optical parametric oscillator," Sci. Rep. **6**, 25245 (2016).
28. G. K. Samanta, G. R. Fayaz, and M. Ebrahim-Zadeh, "1.59 W, single-frequency, continuous-wave optical parametric oscillator based on MgO: sPPLT," Opt. Lett. **32**, 2623–2625 (2007).
29. G. K. Samanta, S. Chaitanya-Kumar, and M. Ebrahim-Zadeh, "Stable, 9.6 W, continuous-wave, single-frequency, fiber-based green source at 532 nm," Opt. Lett. **34**, 1561–1563 (2009).
30. M. V. Jabir, N. Apurv Chaitanya, A. Aadhi, and G. K. Samanta, "Generation of perfect vortex of variable size and its effect in angular spectrum of the down-converted photons," Sci. Rep. **6**, 21877 (2016).
31. G. K. Samanta and M. Ebrahim-Zadeh, "Continuous-wave singly-resonant optical parametric oscillator with resonant wave coupling," Opt. Express **16**, 6883–6888 (2008).
32. J. Arlt, K. Dholakia, L. Allen, and M. J. Padgett, "Parametric down-conversion for light beams possessing orbital angular momentum," Phys. Rev. A **59**, 3950–3952 (1999).